Journal of Materials Chemistry B

Accepted Manuscript

ROYAL SOCIETY OF CHEMISTRY

www.rsc.org/materialsB

Novel Nanosynthesis of In_2O_3 and its Application as a Resistive Gas Sensor for Sevoflurane Anesthetic

M. Karmaoui[a*], S.G. Leonardi[b], D.M. Tobaldi[a], N. Donato[b], R.C. Pullar[a], M.P. Seabra[a], J.A. Labrincha[a], and G. Neri[b]

[a] *Department of Materials and Ceramic Engineering, CICECO, University of Aveiro, Campus Universitário de Santiago, 3810-193 Aveiro, Portugal*

[b] *Dipartimento di Ingegneria Elettronica, Chimica e Ingegneria Industriale, Università di Messina, C.Da Di Dio, 98158 Messina, Italy*

Abstract

A novel non-aqueous sol–gel route for synthesizing pure indium oxide (In_2O_3) nanoparticles (NPs) using indium acetylacetonate and n-butylamine as reactive solvent, under solvothermal condition, is herein proposed. Samples were characterized by advanced X-ray method, whole powder pattern modeling (WPPM) and high-resolution transmission electron microscopy (HR-TEM), showing the exclusive presence of pure In_2O_3. Diffuse reflectance spectroscopy (DRS), was used to determine the optical band gap (E_g) of the sample. Moreover, these investigations also revealed that the In_2O_3 nanoparticles are quasi-spherical in shape, with around 7 nm in diameter as prepared and 9.5 nm after thermal treatment at 250 °C.

In_2O_3 NPs worked as highly sensitive sensing interfaces to provide resistance changes during exposure to sevoflurane, a volatile anesthetic agent used in surgical wards. The developed sensor demonstrated good response and fast response/recovery time towards

very low concentrations of sevoflurane in air, suggesting a very attractive application as real-time monitoring analyzer in hospital ambient.

* Corresponding author. Tel.: +351 234 370 041

E-mail addresses: karmaoui@ua.pt

Introduction

Air pollution in hospital environment, due to accidental emission of hazardous gases, is a serious problem concerning the health of many peoples. An example of this possibility is represented by the administration of volatile anesthetics. To carry out the common surgical practices is required administration of anesthetic in patients with the aim to control pain. Isoflurane, desflurane, enflurane and sevoflurane, a class of volatile halogenated derivates of ethers compounds, together with the nitrous oxide (N_2O) have been the most widely used anesthetics in recent years.[1] Among them, fluoromethyl 2,2,2-trifluoro-1-(trifluoromethyl) ethyl ether commercially known as sevoflurane ($C_4H_3F_7O$), has replaced all the others, making this the most widely used anesthetic in the modern anesthesiology. Actually, because of a series of advantages – quick inhalation induction, rapid recovery, non-pungent odor, and non-irritation of the respiratory system – sevoflurane is a suitable anesthetic agent for mask induction in children and adults.[2,3] However, it is also known that the inhalation of sevoflurane, presents a series of negative effects, such as the induction of seizures, increased blood plasma, onset of delirium and neuromuscular block.[4]

The above problems concern mainly the patients who inhale high concentration of this substance during the surgery, though it has been shown that who works in operating rooms, breathing low concentrations of waste anesthetic vapors, can be directly subject to many others side effects.

According to the U.S. National Institutes of Health (NIH) Office, the recommended time-weighted average occupational exposure limit (OEL) of halogenated gases is 2-20 parts per million.[5] Then, monitoring their concentration, particularly in the surgical wards,where support staff may be exposed, is essential.

In the last years, several different methods were employed to monitor the concentration of sevoflurane in ambient air. For example, it was demonstrated the possibility to use infrared detectors (IR) to monitor low concentrations (0.7-3 ppm) of halogenated anesthetics.[6] However, this and other conventional analytical methods require complicated and expensive instrumentation, professional operators, and complex pre-treatment steps.

At present, in the literature are present few works on the development of versatile and low cost devices for the monitoring of sevoflurane. Okabayashi *et al*.,[7] propose a sevoflurane vapor sensor utilizing cataluminescence of γ-Al_2O_3 catalyst activated with Tb^{3+}. They obtained that the cataluminescence intensity is nearly proportional to the sevoflurane concentration in the range of about 5 to 20 ppm in air by working at 600 °C. Wu *et al*.,[8] developed a resistive sensor based on conductive polypyrrole (Ppy) thick film to detect high concentration of sevoflurane vapor in air at room temperature.

Chavali *et al*.,[9] integrated a sevoflurane sensor based on carbon nanotube-polypyrrole composite (MWCNTs/Ppy) in a compact wireless, active RF (433 MHz) powered device, for the measurement of this anesthetic agent at room temperature.

To date no relevant work reports the use of metal oxide semiconductors for the detection of halogenated anesthetics vapors. Herein we demonstrate the possibility of use of indium oxide (In_2O_3) nanoparticles (NPs) as a sensitive material for the detection of sevoflurane in air.

Metal oxide nanoparticles have been extensively studied and have attracted substantial interest and now play an important role in many areas due to their unique optical, electrical, thermal and catalytic properties.[10] Especially, the unique characteristics such as the large surface-to-volume ratio, excellent catalytic ability and surface activity provide enormous possibilities in improving gas sensing performance.[11] For this scope, different approaches have been made to synthesize metal oxide NPs. A range of increasingly important chemical and physical syntheses for metal, and metal oxide NPs are described in literature.[12–19] Thus, in view of the problems producing metal oxide NPs, it is desirable to develop a simple, efficient and cost-effective method for preparing crystalline nanosized metal oxides. Recently, Ito *et al* established a new route, based on the synthesis of oleic acid-stabilized indium oxide nanocrystals. They synthesized In_2O_3 NPs by means of indium (III) oleate in oleic acid into a large excess of oleyl alcohol, at 230 ºC.[20]

In this study, we developed a novel and facile non-aqueous sol-gel route for producing extraordinary In_2O_3 metal oxide NPs. In_2O_3 NPs are very promising because of their unique properties, such as high electrical conductivity and the possibility of tuning its

band gap by modifying particle size. Furthermore, the reactivity toward several gaseous species has made this material very promising for the realization of gas sensors.

Simplicity of experimental performance, with respect of methods employing aqueous chemistry and/or produced at high temperature, is one of the most important advantages offered by this process. We show that quasi-spherical In_2O_3 NPs can be prepared by the careful use of amine, *via* a facile non-hydrolytic sol-gel route – with good control of the particle size, shape, and crystallinity. The reaction between indium acetyleacetonate (acac = 2,4-pentanedionate) and n-butylamine, at low temperature (140 ºC) for 4 hours, results in the formation of small crystalline In_2O_3 metal oxide NPs. This approach is very convenient, and time-saving; it also requires no capping agent, nor annealing of the product. Moreover, the microstructure (through advanced X-ray methods), morphology, formation mechanism and gas-sensing properties against sevoflurane of those novel In_2O_3 NPs are fully described.

Results and discussion

Formation mechanism

The reaction between indium and manganese acetylacetonate precursor and long-chain amines was well presented by Seo et al in order to produce MnO and In_2O_3.[21,22] Here, we present similar strategy by using a short–chain amine to synthesize indium metal oxide nanoparticle. Low-temperature (140 ºC) synthetic pathways result in direct crystallization of In_2O_3 metal oxide nanoparticles (NPs).

Based on NMR analysis, a mechanism involving the formation of the as synthesized In_2O_3 NPs by the solvothermal process is proposed (**Scheme 1)**.

The proposed mechanism was supported by ^{13}C NMR. The NMR analysis/spectra provide strong evidence to support the proposed mechanism, and significant amount of organic species results were found after the synthesis including n-Butylamine, 4-(butylamino)pent-3-en-2-one, N-butylpropan-2-imine, N-butylacetamide.

Following the proposed mechanism, the formation is based in consecutive steps which involve first the aminolysis of the carbonyl group of the indium acetylacetonate precursor with an amine (1), creating indium-amine complex (2) (after rearrangement) *via* a nucleophilic attack, yields the indium elongate ligand (3) and N-butylacetamide (4). Next step, another amine could nucleophilic attack indium elongate ligand (5) to break the InO complex, resulting in a formation of hydroxyl group (6), and N-butylpropan-2-imine elimination (7). The latter was detected by NMR analysis. In the second step, the hydroxyl group of (2) was nucleophilic attack to indium site in indium acetylacetonate (1), forming bridging oxo group under acetylacetone species elimination likewise leads to In-O-In bridges (the oxide formation). The acetylacetone was condensed with another amine to produce 4-(butylamino)pent-3-en-2-one, as already confirmed by NMR analysis. The product of this reaction is already observed for various metal oxides synthesized in benzyl amine, and detailed formation mechanisms of iron oxide nanoparticles *via* non-hydrolytic approach is available in an aforementioned reference.[21]

The as-prepared In_2O_3 NPs were then thermally treated at 250 °C, *i.e.* in the same conditions adopted to pretreat the In_2O_3 NPs sensing layer before the sensing tests.

This is to ensure that no further structural rearrangement can occur during operation of the sensor.

X-ray characterization: structure and microstructure

A graphical output of the Rietveld crystal structural refinement for the as prepared and thermal treated samples is depicted in **Figure 1a-b**, while the crystal structural data, as well as a 3D visualization of its crystal structure – attained with the VESTA software package,[23] and inserting the structural data (bond lengths, bond angles, atomic positions and U_{iso}) obtained from GSAS – are in Table 1, and inset of **Figure 1a**. In^{3+} is octahedrally coordinated and accommodated in two crystallographically distinct sites: 24 cations are at Wyckoff position 24(*d*), having C_2 point symmetry (here referred to as site *In1*), whilst eight cations in 8(*b*), with D_{3d} point symmetry (site *In2*).[24] The octahedral sites ($In1O_6$ and $In2O_6$) distortion was evaluated considering the distortion index of the octahedral site *D*, as defined by Baur.[25] Moreover, also the octahedral quadratic elongation ($OQE = <\lambda>$), and the bond angle variance ($BAV = \sigma^2$) were used for a further evaluation of the octahedral site distortion.[26] As reported in Table 1, the *In2* site is much more regular compared to *In1* – the *In2*–O bond lengths (apical and basal) being the same, hence their Baur indices *D* are nil. The thermal treatment at 250 °C leads to a slight increase in the distortion (quadratic elongation) of *In1* site. Whilst both *In1* and *In2* sites seems to have a greater bond-angle distortion, consequently to the thermal treatment.

The sizes and size distributions were provided by advanced X-ray powder diffraction (XRPD) technique – *i.e.* by way of the WPPM method. The crystalline domain size distribution of the as synthesized and thermal treated samples In_2O_3 is reported in

Figure 2a-b, whilst a graphical output of the WPPM modeling is shown in the inset of **Figure 2a-b**. The agreement factors and the microstructural data of the WPPM modeling are reported in Table 2. From this XRD analysis, the average crystalline domain diameter of as-prepared In_2O_3 was found to be 7.0 nm, with a narrow size distribution, the mode being 4.8 nm. In Figure 2b, is shown the size distribution and the graphical output of WPPM modeling of the In_2O_3 thermally treated at 250 °C. As it is seen (*cf* also Table 2), the thermal treatment causes a slight increase in the unit cell parameters and in the average domain diameter (9.5 nm *versus* 7.0 nm). Also, the size distribution appears narrower, being its mode at 8.4 nm; it is interesting to note that there are no detected domains with $\langle D \rangle < 2.5$ nm.

TEM characterization

The morphological characteristics of the In_2O_3 NPs were investigated by transmission electron microscopy (TEM), and high-resolution transmission electron microscopy analysis (HR-TEM). As shown in **Figure 3a**, the small NPs of In_2O_3 obtained after synthesis are quite regular in shape, and sub-spherical. The corresponding selected area electron diffraction (SAED) pattern (inset of **Figure 3a**) shows the typical diffraction rings which can be indexed to the In_2O_3 phase. HR-TEM images show the presence of well dispersed and homogeneous NPs spherical in shape as shown in the **Figure 3b**. High resolution images recorded from these In_2O_3 NPs reveal that they are constituted of well-defined **5–7** nm primary particles, which agree well with the crystalline domain

diameter derived from the XRPD study, hence confirming the results obtained *via* the WPPM method. The FFT pattern of In_2O_3 NPs is shown in the inset of **Figure 3b**.

HR-TEM image of In_2O_3 NPs is presented in detail in the **Figure 3 c-d**. FFT patterns, and well-defined spots which are in agreement with the crystallographic parameters for the In_2O_3 NPs signifying that the NPs were highly crystalline. Lattice fringes with a spacing of 1.78 Å are visible, corresponding to the (440) interplanar distance of indium oxide NPs having cubic symmetry.

In Figure 3e is reported a micrograph recorded from the thermal treated In_2O_3 NPs. The average particles size, as calculated taking into account many particles coming from different micrographs, is 9-10 nm slightly higher than that of untreated sample. Figure 3f shows clearly the lattice planes of a single highly crystalline In_2O_3 nanoparticles. The measured fringe spacing value is 2.93 Å, which corresponds to the spacing between (222) lattice planes of the In_2O_3.

Sensing tests

In_2O_3 nanoparticles show very interesting properties for gas sensing. In particular, In_2O_3 NPs synthesized by non-aqueous processes demonstrated superior sensing performances.[27–30]

Here, the sensing behavior of In_2O_3 NPs prepared by the solvothermal process described was investigated in the monitoring of sevoflurane. First, sensing performance toward sevoflurane was investigated at different temperatures in order to define the optimal operation condition. **Figure 4** shows the sensor response at different operation temperatures evaluated allowing the film to stabilize its resistance when exposed to

target gas. In the range investigated the response increases with temperature showing a maximum at 100 °C. The high sensitivity and fast response observed, could be ascribed to large specific surface and electron confinement due to small particle size of In_2O_3 NPs.[31] However, at this temperature and until 150 °C, an incomplete recovery of the baseline was observed. Indeed, after each pulse of sevoflurane the resistance baseline is not recoverable at all (**Figure 5a**). This behavior can be due to the irreversible adsorption of sevoflurane and/or its reaction products on the sensing layer, that might block the site for oxygen adsorption and consequently lead to a permanent reduction of resistance. A similar effect on In_2O_3-based sensor has been observed during monitoring of carbonyl sulphide.[32]

At operating temperature higher than 150 °C, there is instead enough energy to promote desorption of these species. **Figure 5b** shows the dynamic behavior evaluated at 250 °C for the sensor exposed to 1.5 ppm of sevoflurane. It is observed a reduction of the resistance when the target gas is pulsed into the test chamber. This behavior is in agreement with the functioning principle of n-type semiconductor sensing materials when interact with reducing gases. It involves the chemisorbed oxygen ions, such as O_2^-, O^- and O^{2-} on the surface of In_2O_3, which trap the electrons from the bulk, leading to the formation of a high potential barrier at grain boundary interface.[33] As the sevoflurane vapor was injected, it reacts with oxygen that are adsorbed on the surface of the grains, resulting in the release of electrons into the bulk. In a n-type semiconductor, this leads to reduction of the potential barrier, and then to a decrease of resistance of In_2O_3 film. As confirmed by electrochemical investigations about halogenated anesthetic agent, the reaction mechanisms involve direct interaction between organic halides and

superoxide species to produce peroxide.[34–36] For indium oxides, superoxide species are represented by chemisorbed oxygen ions, then it can promote direct oxidation of sevoflurane on grains surface. Further, complete recovery of the baseline observed when the target gas is out, indicates reversible interaction with sevoflurane molecules. Response time t_{S90} (time to reach 90% of its final stable signal in presence of target gas), and recovery time t_{R90} (time to reach 90% of the baseline signal after target gas is removed), are 15 and 30 seconds, respectively.

Fast dynamic response makes the developed sensor suitable to work in pulsed mode, as well as with a flow injection analysis (FIA) system. As regards the pulse mode operation, this technique is superior to standard procedure as demonstrated by Martinelli et al. [E. Martinelli et al., Short time gas delivery pattern improves long-term sensor reproducibility, Sensors and Actuators, B: Chemical 156,753-759, 2011]. The better performance of pulse mode is related to the fact that the amount of adsorbed molecules is smaller with respect to the standard equilibrium measurements. This reduces the probability of poisoning of the sensing layer surface making more efficient the re-initialization of the sensor. In **Figure 6a** is shown the transient response of the sensor at 250 °C for different pulses ranging from 1.5 to 14 ppm of sevoflurane vapor in air. The duration of each pulse is about 15 seconds, therefore, enough to allow the sensor to reach approximately 90% of the maximum response. The spike observed during the recovery phase for each pulse, is due to the switching of the valve to return to the reference gas. The lower detection limit estimated by calibration curve, showed in **Figure 6b**, is less than 500 ppb of sevoflurane. As reported in **Figure S3**, showing the response of the sensor to successive pulses of the same concentration of sevoflurane, it

can be noted a high reproducibility of response over time, retained even after many subsequent work cycles.

Long-term stability, negligible humidity interference and cross sensitivity are important requisite for the practical application of sensors. In this respect, one of the limiting aspects when working with metal oxide nanoparticles is their thermal stability. TGA (see Fig. S4) was then performed to investigate the thermal behavior of the as-prepared In_2O_3 NPs, which is helpful to acquire information about the stability of the sensor device. In the range RT-300 °C, a slight decrease of weight was observed (less 4 wt%), attributed to the adsorbed moisture and organic solvent and removal/oxidation of organic species adsorbed. No significant weight loss was noted at higher temperature giving evidences for the absence of carbon or other residual impurities above this temperature. Concerning the sensor device, no remarkable degradation of the sensing performances has been noted during a prolonged testing period (around one month), indicating also that the pretreatment procedure adopted was sufficient to ensure the necessary mechanical and structural stability of the sensing layer. During this period, the variation of baseline resistance in air (baseline drift) was less of 5%, whereas the relative standard deviation of the response to 1.5 ppm of sevoflurane was estimated to be less than 7%.

It is well known that that humidity plays an important role in sensing mechanism; even at low values, humidity acts interfering with sensor response. Furthermore, chemical sensors based on metal oxides suffer of low selectivity, which limits their practical applications. The examination of the water influence and cross-sensitivity was out of the scope of the present paper and will be investigated in a forthcoming work aimed to

optimize the sensor performance for developing a practical device for the application considered.

Conclusion:

We reported an innovative and original reaction process retaining a non-hydrolytic procedure to synthesize nanocrystalline In_2O_3 metal oxide nanoparticle, with about 7 nm in diameter.

This new non-aqueous sol-gel route presented an efficient process to synthesize nanosized In_2O_3 particles through a solvothermal approach, by using indium (acetyleacetonate) metal oxide precursor as a single precursor, and n-butyamine as a reactive solvent. Formation of the In_2O_3 NPs was governed by the use of amine, so as to direct this nanosized morphology. Moreover, a quantitative XRPD microstructural analysis, *via* the WPPM method – used for the first time in this system – and HR-TEM, gave detailed information about the shape, size and size distribution of the semiconductor.

Moreover, we verified that In_2O_3 NPs can be a potential material platform which serves as a gas sensing layer for the monitoring of sevoflurane, a volatile anesthetic. The developed sensor possessed high response, and also very fast response and recovery time, and can therefore be used for monitoring this substance in surgical wards.

Experimental section:

2.1 Chemicals and materials:

Indium (III) acetylacetonate [$In(OCCH_3CHOCCH_3)_3$] (≥99.99%) trace metals basis, and n-butylamine (99.5%) [$CH_3(CH_2)_3NH_2$] were used, all from Aldrich.

2.2 Synthesis of In_2O_3 nanoparticles:

The synthesis was carried out in a glovebox (O_2 and H_2O < 1 ppm). In a typical procedure, 1 mmol (0.5 g) of indium (III) acetylacetonate [$In(OCCH_3CHOCCH_3)_3$] were added to 15 mL of n-butylamine, the reaction mixture was transferred into a stainless steel autoclave, and carefully sealed. The autoclave was taken out of the glove-box, and heated in a furnace at 140 ºC for 4 hours. The resulting milky suspensions were centrifuged, and the precipitates were thoroughly washed with ethanol and dichloromethane, and dried in air at 60 ºC.

The as prepared In_2O_3 was thermally treated in air (2 hours at the maximum temperature of 250 °C).

2.3 Sample characterization:

X-ray powder diffraction (XRPD) data were collected using a laboratory θ/θ diffractometer, PANalytical X'Pert Pro (NL), equipped with a fast RTMS detector (PANalytical PIXcel 1D), with Cu Kα radiation (40kV and 40 mA, 15-115 °2θ range, a virtual step scan of 0.02 °2θ and virtual time per step of 500 s). The incident beam pathway was as follows: 0.125° divergence slit, 0.125° anti-scattering slit, 0.04 rad soller

slits, and a 15 mm copper mask. The pathway of the diffracted beam included a Ni filter, soller slits (0.04 rad), and an antiscatter blade (5 mm).

The Rietveld crystal structural refinements were carried out with the GSAS software package, together with its graphical interface EXPGUI.[37,38] The starting atomic parameters for In_2O_3, described in the space group (SG) $Ia\bar{3}$, were taken from Bartos *et al*.[24] This strategy was followed for the refinement: scale-factors, zero-point, 6 coefficients of the shifted Chebyshev function to fit the background, unit cell parameters and also profile coefficients – one Gaussian (GW), an angle-independent term, and two Lorentzian terms, L_X and L_Y – atomic positions, and isotropic displacement parameters (U_{iso}). The microstructural refinement was assessed on the same XRPD data, *via* the whole powder pattern modeling (WPPM) procedure,[39,40], through the PM2K software (assessed for the first time in the In_2O_3 system):[41] this method allows for refinement of model parameters *via* a non-linear least squares procedure. This is believed to be a state-of-the-art methodology, and permits to extract microstructural information from a diffraction pattern. This way, the experimental peaks are fitted without any use of arbitrary analytical function (like Gaussian, Lorentzian, or Voigtian functions), being the diffraction peak profile the result of a convolution of instrumental and sample-related physical effects. Consequently, the analysis is directly made in terms of physical models of microstructure and/or lattice defects. Hence, with the WPPM formalism, aspects of In_2O_3 microstructure, as the crystalline domain shape and size distribution, can be reliably studied, compared to other integral breadth methods that are frequently used for line profile analysis (LPA), like the mostly used Scherrer formula,[42] or the Williamson–

Hall method.[43] Actually, in these latter methods,[42,43] instrumental profile component, background and peak profile overlapping, can make difficult to correctly extract integral breadths; also additional sources of line broadening – that can be: domain size, lattice strain and layer faulting – can not be considered properly.[44]

The instrumental contribution was obtained by modeling (using the same software) 14 *hkl* reflections from the NIST SRM 660b standard (LaB_6), according to the Caglioti *et al*. relationship.[45] Afterward, In_2O_3 (SG $Ia\bar{3}$) was included in the WPPM modeling, and these parameters were refined: background – modeled using a 4th-order of the shifted Chebyshev polynomial function – peak intensities, lattice parameters, and specimen displacement. Crystalline domains were assumed to be spherical, and distributed according to a lognormal size distribution.

Diffuse reflectance spectroscopy (DRS), was used to estimate the optical band gap (E_g) of the obtained oxide. Spectra were acquired on a Shimadzu UV 3100, in the UV-Vis range (825-250 nm), with 0.2 nm in step-size, and using an integrating sphere and white reference material, both made of $BaSO_4$. The Tauc's procedure was used with the aim of estimating the optical E_g of In_2O_3; at this purpose, the diffuse reflectance (R_∞) was converted into the absorption coefficient α, using the Kubelka–Munk equation – $\alpha = (1 - R_\infty)^2 \times 2R_\infty^{-1}$.[46]

Transmission electron microscopy (TEM) was performed using a Jeol-2000 FXII microscope, with point-to-point and line-to-line resolutions of 0.28 nm and 0.14 nm, respectively. High resolution TEM (HR-TEM) was performed using a JEOL 2200FS microscope with a field emission gun, operated at 200 kV. Samples for TEM / HR-TEM

observations were prepared by dispersing the NPs in ethanol and evaporating the suspension drops on carbon-coated copper grids.

Thermal analysis; carried out with a heating rate of 10 °C/min in flowing air up to 400 °C, was performed by using a TG-DSC Netzsch Model STA409PC instrument.

2.4 Sensor fabrication:

The bare sensor used consists of an alumina substrate (dimension of 6 × 3 mm), provided with a pair of platinum interdigitated electrodes on the front and a platinum heater and back side (Fig. S5a). In_2O_3 aqueous paste was then screen printed on the interdigitated electrodes in order to print a thick layer (1-10 μm). Finally, after drying at room temperature till the complete water evaporation, a sensing layer highly adherent to the substrate was obtained. Fig. S5b shows the sensor mounted into the holder and ready to be used for the gas sensing tests.

2.5 Sensing tests and apparatus:

The experimental bench for gas sensing tests allowed to carry out measurements in controlled atmosphere and temperature. Carrier gas was pure dry air coming from a bottle; instead, sevoflurane vapor was obtained by means of a certified permeation tube maintained at controlled temperature in a thermostatic bath. Several concentrations of sevoflurane were prepared by diluting anesthetic vapor coming from permeation tube, with air, using two mass flow controllers. The concentration of target gas was varied in range 1.5-14 ppm. Before sensing tests the sensor was conditioned at 250 °C until a

stable baseline was attained. The sensor was tested at various operation temperatures, 50-250 °C, by changing the current flowing through platinum heater place on the back side of the substrate.

The dynamic flow system used a sample injection analysis method (FIA). A sample loop of 13 mL volume, was filled with a mixture at different concentration of sevoflurane vapor in air. By actuating a valve the mixture was injected into the sensor chamber. The flow rate of the carrier gas was fixed at 100 mL/min during all measurements.

A multimeter data acquisition unit Agilent 34970A was used for acquisition the electrical resistance of the In_2O_3 film, while a dual-channel power supplier instrument Agilent E3632A was employed to bias the built-in heater of the sensor to perform measurements at super-ambient temperatures.

The gas response, S, is defined as $S = [R_0/R]$ where R_0 is the baseline resistance in dry air and R is the electrical resistance of the sensor at different sevoflurane concentration.

Acknowledgements

Mohamed Karmaoui thanks Fundação para a Ciência e a Tecnologia (FCT) for grant Nº SFRH/BPD/74477/2010. D.M. Tobaldi is grateful to the ECO-SEE project (European Union's Seventh Framework Programme funding, grant agreement no 609234). Mohamed Karmaoui thanks Prof. Artur Silva and Reda Ahmed for NMR measurements and their fruitful discussions (University of Aveiro, Portugal). Authors acknowledge PEst-C/CTM/LA0011/2013 programme. M.P. Seabra and R.C. Pullar wish to thank the FCT Ciência2008 programme for supporting this work.

References:

[1] J. S. Yasny, J. White, *Anesth. Prog.* **2012**, *59*, 154.

[2] F. Michel, J.-M. Constantin, *Expert Opin. Pharmacother.* **2009**, *10*, 861.

[3] C. J. Young, J. L. Apfelbaum, *J. Clin. Anesth.* **1995**, *7*, 564.

[4] E. M. Sakai, L. A. Connolly, J. A. Klauck, *Pharmacother. J. Hum. Pharmacol. Drug Ther.* **2005**, *25*, 1773.

[5] NIH Waste Anesthetic Gas WAG Surveillance Program 2012, National Institutes of Health . Office of Research Services . Division of Occupational Health and Safety http://www.ors.od.nih.gov.

[6] H. Rasmussen, S. Thorud, *J. Am. Assoc. Lab. Anim. Sci. JAALAS* **2007**, *46*, 64.

[7] T. Okabayashi, M. Ozaki, M. Nakagawa, *Procedia Eng.* **2011**, *25*, 1093.

[8] R.-J. Wu, Y.-C. Huang, M. Chavali, T. H. Lin, S.-L. Hung, H.-N. Luk, *Sens. Actuators B Chem.* **2007**, *126*, 387.

[9] M. Chavali, T.-H. Lin, R.-J. Wu, H.-N. Luk, S.-L. Hung, *Sens. Actuators Phys.* **2008**, *141*, 109.

[10] J. A. Rodríguez, M. Fernández Garcia, *Synthesis, properties, and applications of oxide nanomaterials*; Wiley-Interscience: Hoboken, N.J., 2007.

[11] M. E. Franke, T. J. Koplin, U. Simon, *Small Weinh. Bergstr. Ger.* **2006**, *2*, 36.

[12] X. Sun, H. Hao, H. Ji, X. Li, S. Cai, C. Zheng, *ACS Appl. Mater. Interfaces* **2014**, *6*, 401.

[13] R. A. Gilstrap, C. J. Capozzi, C. G. Carson, R. A. Gerhardt, C. J. Summers, *Adv. Mater.* **2008**, *20*, 4163.

[14] M. Epifani, R. Díaz, J. Arbiol, E. Comini, N. Sergent, T. Pagnier, P. Siciliano, G. Faglia, J. R. Morante, *Adv. Funct. Mater.* **2006**, *16*, 1488.

[15] G. Bühler, D. Thölmann, C. Feldmann, *Adv. Mater.* **2007**, *19*, 2224.

[16] H. Jiang, J. Hu, F. Gu, W. Shao, C. Li, *Chem. Commun.* **2009**, 3618.

[17] K. Soulantica, A. Maisonnat, M.-C. Fromen, M.-J. Casanove, P. Lecante, B. Chaudret, *Angew. Chem. Int. Ed.* **2001**, *40*, 448.

[18] C. Wang, D. Chen, X. Jiao, C. Chen, *J. Phys. Chem. C* **2007**, *111*, 13398.

[19] J. Liu, T. Luo, F. Meng, K. Qian, Y. Wan, J. Liu, *J. Phys. Chem. C* **2010**, *114*, 4887.

[20] D. Ito, S. Yokoyama, T. Zaikova, K. Masuko, J. E. Hutchison, *ACS Nano* **2014**, *8*, 64.

[21] W. S. Seo, H. H. Jo, K. Lee, B. Kim, S. J. Oh, J. T. Park, *Angew. Chem. Int. Ed.* **2004**, *43*, 1115.

[22] W. S. Seo, H. H. Jo, K. Lee, J. T. Park, *Adv. Mater.* **2003**, *15*, 795.

[23] K. Momma, F. Izumi, *J. Appl. Crystallogr.* **2008**, *41*, 653.

[24] A. Bartos, K. P. Lieb, M. Uhrmacher, D. Wiarda, *Acta Crystallogr. B* **1993**, *49*, 165.

[25] W. H. Baur, *Acta Crystallogr. B* **1974**, *30*, 1195.

[26] K. Robinson, G. V. Gibbs, P. H. Ribbe, *Science* **1971**, *172*, 567.

[27] N. Pinna, M. Niederberger, *Angew. Chem. Int. Ed.* **2008**, *47*, 5292.

[28] M. Niederberger, G. Garnweitner, N. Pinna, G. Neri, *Prog. Solid State Chem.* **2005**, *33*, 59.

[29] G. Neri, A. Bonavita, G. Micali, G. Rizzo, S. Galvagno, M. Niederberger, N. Pinna, *Chem. Commun.* **2005**, 6032.

[30] G. Neri, A. Bonavita, G. Micali, G. Rizzo, N. Pinna, M. Niederberger, *Sens. Actuators B Chem.* **2007**, *127*, 455.

[31] V. N. Singh, B. R. Mehta, R. K. Joshi, F. E. Kruis, *J. Nanosci. Nanotechnol.* **2007**, *7*, 1930.

[32] G. Neri, A. Bonavita, S. Ipsale, G. Micali, G. Rizzo, N. Donato, In *IEEE International Symposium on Industrial Electronics, 2007. ISIE 2007*; 2007; pp. 2776–2781.

[33] Z. Guo, J. Liu, Y. Jia, X. Chen, F. Meng, M. Li, J. Liu, *Nanotechnology* **2008**, *19*, 345704.

[34] S. Floate, C. E. W. Hahn, *Sens. Actuators B Chem.* **2003**, *96*, 6.

[35] S. Floate, C. E. W. Hahn, *Sens. Actuators B Chem.* **2004**, *99*, 236.

[36] M. J. Moorcroft, C. E. W. Hahn, R. G. Compton, *J. Electroanal. Chem.* **2003**, *541*, 117.

[37] A. C. Larson, R. B. Von Dreele, *General Structure Analysis System (GSAS)*; Los Alamos National Laboratory Report LAUR, 2004.

[38] B. H. Toby, *J. Appl. Crystallogr.* **2001**, *34*, 210.

[39] P. Scardi, M. Leoni, *Acta Crystallogr. A* **2002**, *58*, 190.

[40] P. Scardi, M. Leoni, In *Diffraction Analysis of the Microstructure of Materials*; Eric J. Mittemeijer, Paolo Scardi: Berlin, 2004; pp. 51–92.

[41] M. Leoni, T. Confente, P. Scardi, *Z. Für Krist. Suppl.* **2006**, *23*, 249.

[42] H. P. Klug, L. E. Alexander, *X-Ray Diffr. Proced. Polycryst. Amorph. Mater. 2nd Ed. Harold P Klug Leroy E Alexander Pp 992 ISBN 0-471-49369-4 Wiley-VCH May 1974* **1974**, *-1*.

[43] G. K. Williamson, W. H. Hall, *Acta Metall.* **1953**, *1*, 22.

[44] P. Scardi, M. Leoni, *Acta Mater.* **2005**, *53*, 5229.

[45] G. Caglioti, A. Paoletti, F. P. Ricci, *Nucl. Instrum. Methods* **1960**, *9*, 195.

[46] A. S. Marfunin, *Physics of Minerals and Inorganic Materials: An Introduction*; Springer-Verlag, 1979.

Scheme 1. - Proposed reaction mechanism occurring during the non-aqueous synthesis of In_2O_3 oxide NPs in butylamine.

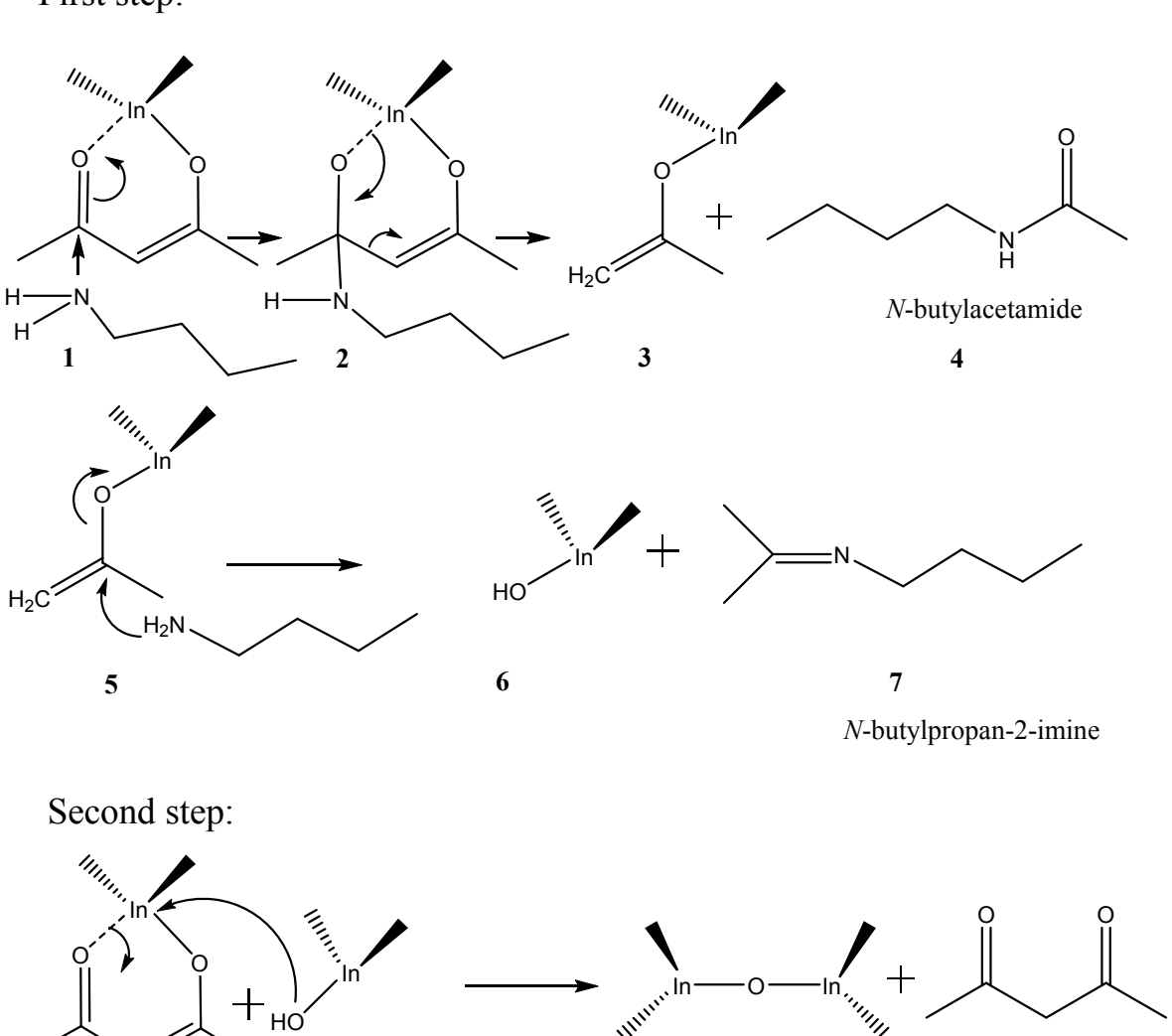

Figure 1 – Graphic output of the Rietveld refinement of: a) as synthesized In_2O_3 and b) In_2O_3 thermally treated at 250 °C. The black open squares represent the calculated pattern, the continuous red line represents the observed pattern, and the difference curve between observed and calculated profiles is the blue continuous line plotted below. The positions of reflections are indicated by the small vertical bars. In the inset of Figure 1a is shown a 3D visualization of In_2O_3 crystal structure. The small dark grey spheres represent oxygen, the (bigger) violet spheres, indium.

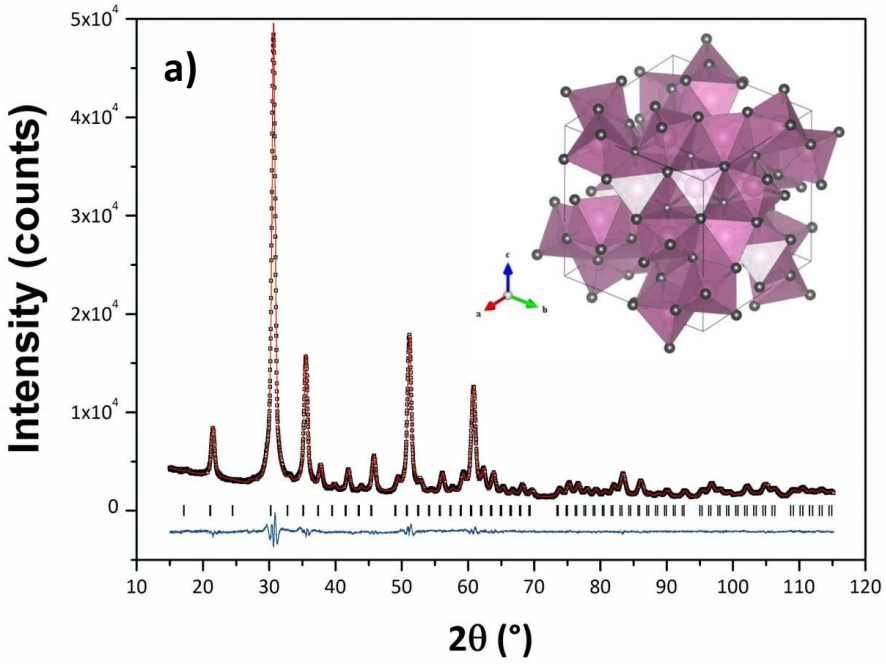

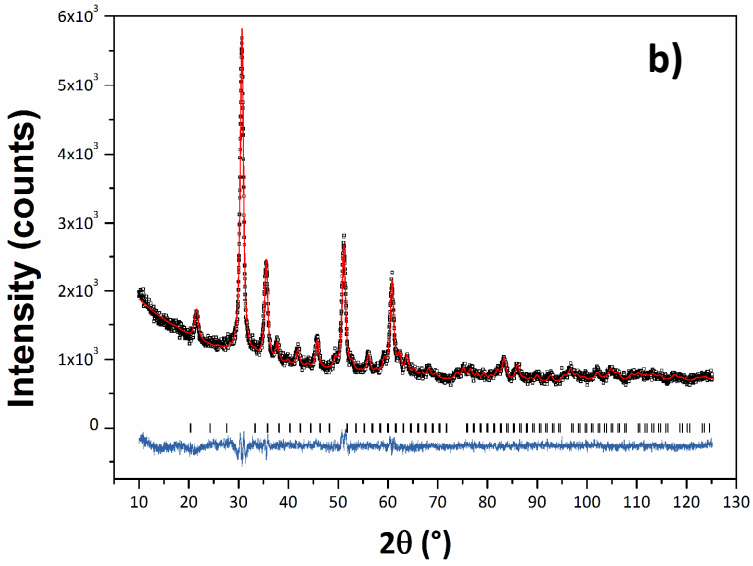

Table 1

Agreement factors of the Rietveld refinements, distortion indices (*D*), quadratic elongation (*QE*), and bond angle variance (*BAV*) of InO_6 octahedra (*In1* and *In2* sites).

Sample	No. of variables	Agreement factors				*D*		*QE*		*BAV* (^{o2})	
		$R(_F^2)$ (%)	R_{wp} (%)	χ^2		*In1*	*In2*	*In1*	*In2*	*In1*	*In2*
In_2O_3	19	1.79	3.35	3.58		0.028(1)	0	1.066(1)	1.024(1)	191.5(1)	74.8(1)
In_2O_3@250	15	3.74	4.55	1.94		0.028(1)	0	1.070(1)	1.025(1)	207.0(1)	79.1(1)

Note: there were 4987 observations; the number of In_2O_3 reflections in the data set was 244.

Figure 2 – Crystalline domain size distribution of: a) as synthesized In_2O_3 and b) In_2O_3 thermally treated at 250 °C. The graphical output of the WPPM modeling of In_2O_3 (black open squares are observed data, red continuous line the calculated data, and the lower blue continuous line is the difference curve between observed and calculated profiles) is shown in the inset.

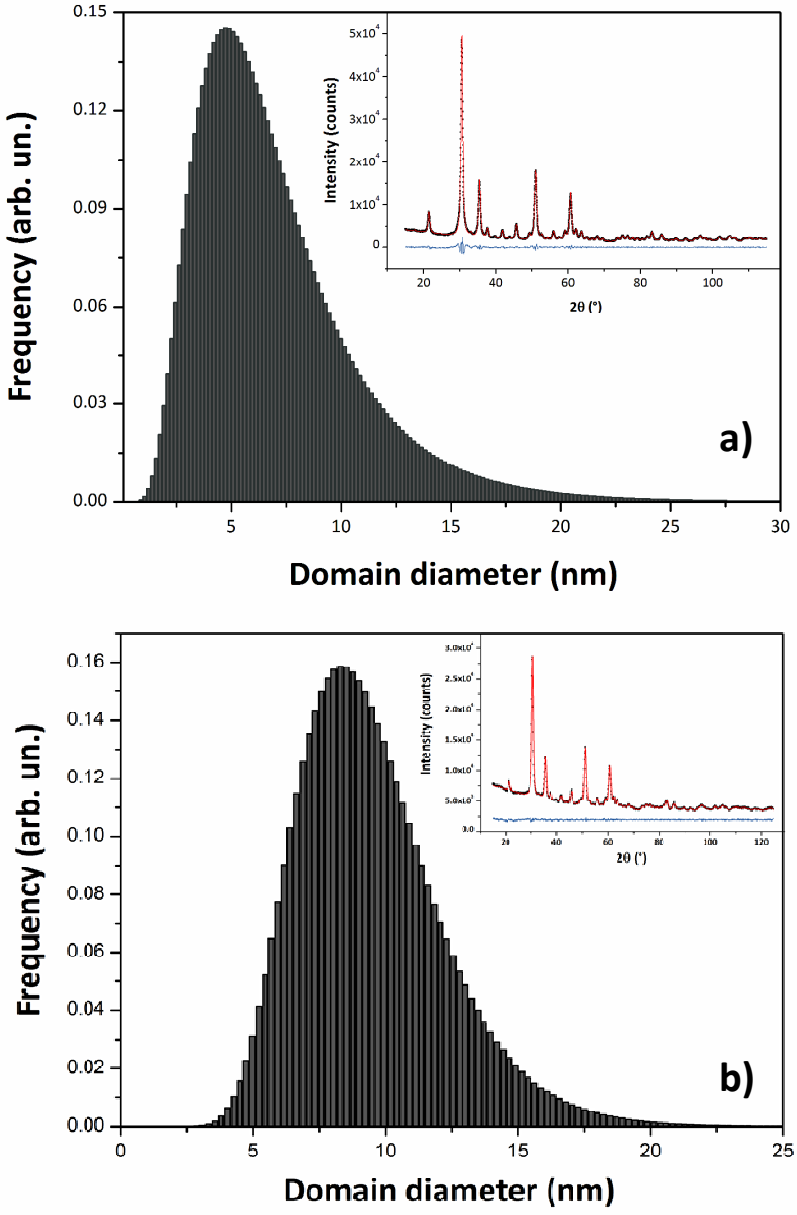

Table 2

WPPM agreement factors, unit cell parameters, average crystalline domain diameter, and mode of the size distribution.

Sample	Agreement factors				Unit cell parameters (nm), $a = b = c$	Average crystalline domain diameter (nm)	Mode of the size distribution (nm)
	R_{wp} (%)	R_{exp} (%)	χ^2				
In_2O_3	3.73	1.77	2.11		1.01168(1)	7.0(1)	4.8(1)
In_2O_3@250	1.83	1.38	1.32		1.01214(5)	9.5(3)	8.4(3)

Figure 3 TEM image of the In_2O_3 NPs synthesized at 140 °C (a), and HR-TEM image of an assembly of In_2O_3 NPs (b and c). Both the inset in (a and b) are the corresponding SAED pattern. HR-TEM image of In_2O_3 NPs; the inset in (d) depicts the FFT analysis of the marked area with red square. The parallel red lines in (d) show a *d*-spacing of 1.78 Å for the (440) plane. TEM image of the In_2O_3 thermally treated at 250 °C (e), and HR-TEM image of a single particle showing a *d*-spacing of 2.93 Å for the (222) lattice plane.

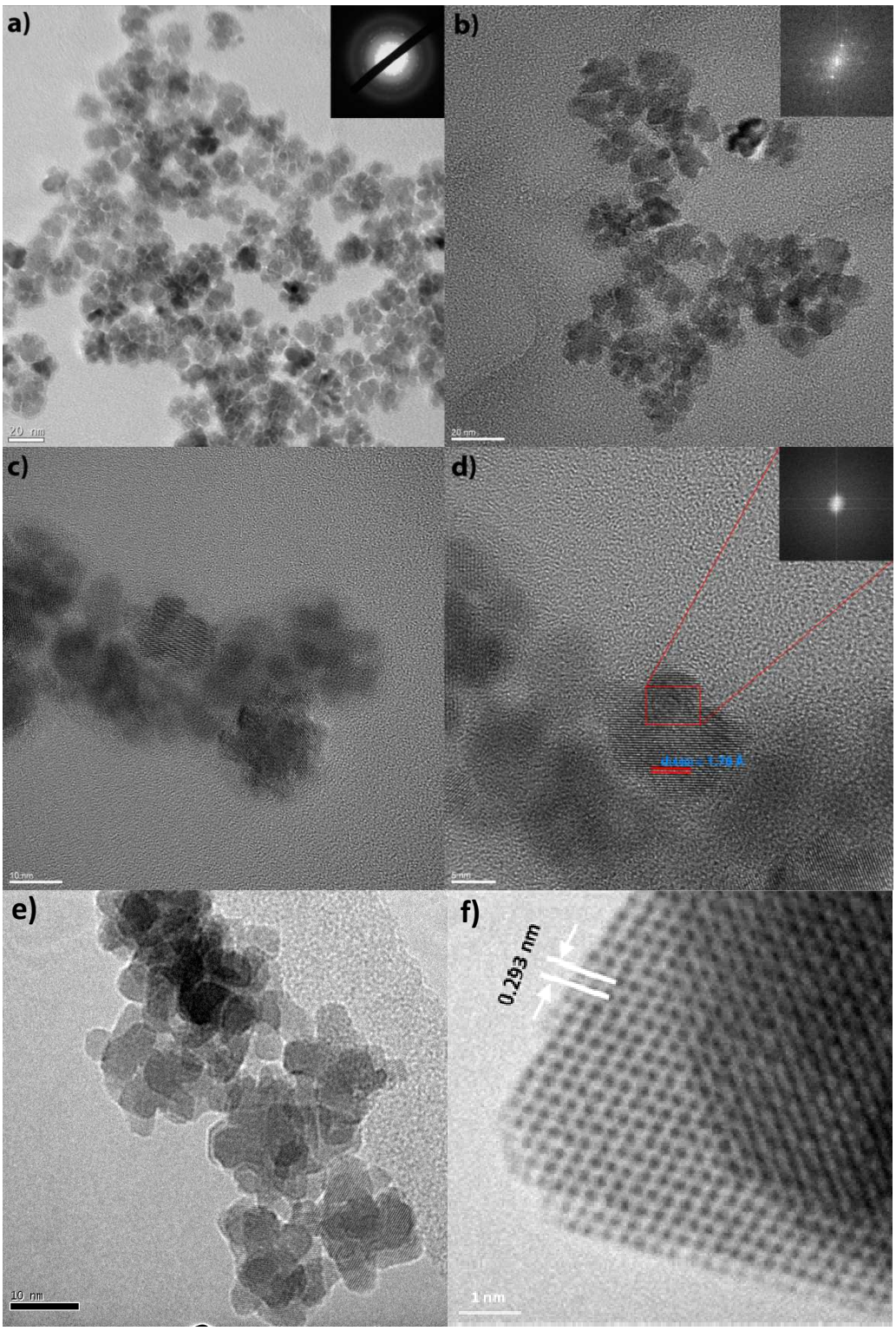

Figure 4 Sensor response at 1.5 ppm of sevoflurane in air at different operating temperatures.

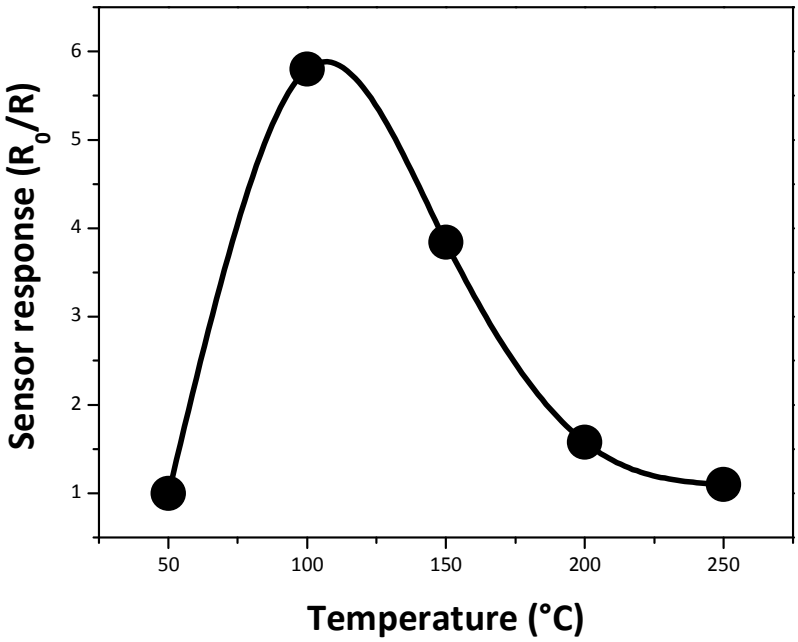

Figure 5 Dynamic responses (a) 150 °C, (b) 250 °C, of the sensor at two pulse of 1.5 ppm of sevoflurane.

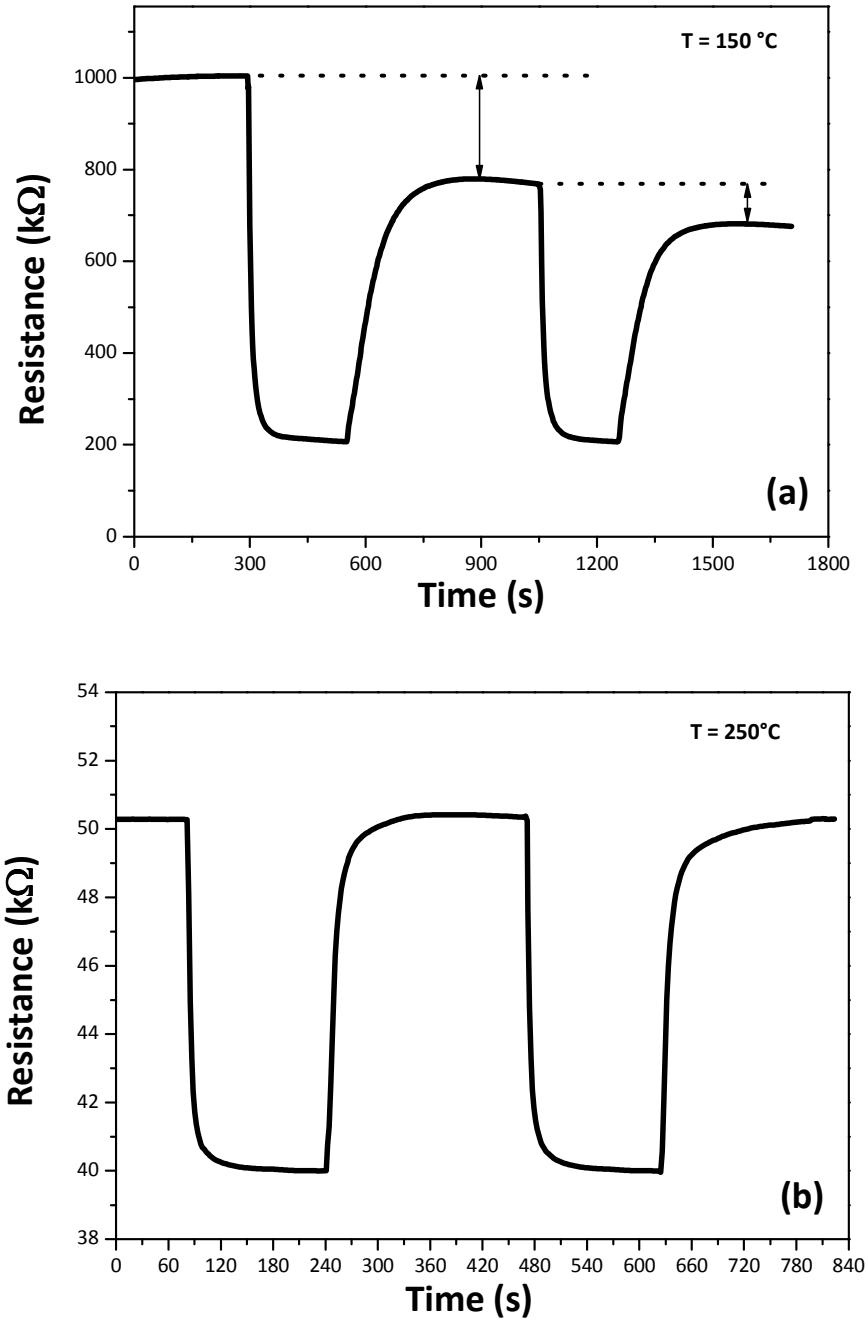

Figure 6 Dynamic response of the sensor (a) obtained with FIA system for different concentration of sevoflurane in air at operation temperature of 250 °C, and relative calibration curve (b).